The Autonomous Underwater Glider "Spray"

Jeff Sherman, Russ E. Davis, W. B. Owens, and J. Valdes

***Abstract*—A small (50-kg, 2-m long) underwater vehicle with operating speeds of 20–30 cm/s and ranges up to 6000 km has been developed and field tested. The vehicle is essentially an autonomous profiling float that uses a buoyancy engine to cycle vertically and wings to glide horizontally while moving up and down. Operational control and data relay is provided by GPS navigation and two-way communication through ORBCOMM low-earth-orbit satellites. Missions are envisioned with profile measurements repeated at a station or spaced along a transect. The initial instrument complement of temperature, conductivity, and pressure sensors was used to observe internal waves and tides in the Monterey underwater canyon.**

***Index Terms*—Autonomous glider, remote sensing, satellite communication, underwater vehicles.**

I. Stommel's Vision

In 1989, a year before the first autonomous floats were placed in service, Henry Stommel published a far-thinking article [11] envisioning a world ocean-observing system based on "a fleet of 1000 small neutrally-buoyant floats called Slocums" that "migrate vertically through the ocean by changing ballast, and they can be steered horizontally by gliding on wings at about a 35 degrees angle… . During brief moments at the surface, they transmit their accumulated data and receive instructions… . Their speed is generally about 0.5 knot." The name Slocum commemorated Joshua Slocum who first sailed around the world alone.

Today, a decade later, most of what Stommel envisioned is becoming reality. The Argo program is implementing a 3000-float array of temperature and salinity profilers although, unlike Stommel's Slocums, the Argo floats' positions cannot be controlled. Modern satellite technology has simplified positioning and made feasible two-way relay of data and instructions. As part of the ONR-sponsored Autonomous Ocean Sensing Network (AOSN) program, three groups in the U.S. are developing the concept of winged gliders propelled by buoyancy engines to bring to fruition another part of Stommel's vision. Even the Slocum concept of powering the buoyancy engine from the ocean's thermal stratification has been demonstrated in prototype by Stommel's neighbor and friend, Doug Webb of the Webb Research Corporation (WRC).

Our purpose here is to report the development and initial use of a buoyancy-engine-powered underwater glider designed for long-term (∼year) missions requiring the ability to move several thousand kilometers at speeds near 25 cm/s. Making clear its connection to Stommel's vision, our autonomous vehicle is named "Spray" after the boat Joshua Slocum rebuilt and piloted around the world. This small (∼2-m length and 50-kg mass) submarine is inexpensive enough (∼$25 000) to be used in large numbers. The Global Positioning System (GPS) permits rapid locating when the vehicle surfaces, and efficient two-way ORBCOMM satellite communication supports transfer of several kilobytes of data per day and allows the vehicle's mission to be changed in response to measurements taken.

Just as the Slocum concept was informed by development of the Autonomous Lagrangian Circulation Explorer [13], so the Spray development owes more to Stommel than simply the Slocum concept. As the design and manufacturing problems in ALACE were being worked on, Stommel and Webb had begun to design and develop the Slocum. They built an operating thermally driven buoyancy engine that Stommel was known to demonstrate to guests at his home. They also developed a basic configuration for gliders that we have adopted, most importantly the idea of controlling underwater flight by moving ballast in the manner of a hang glider. By 1991, preliminary lake tests of a vehicle had been carried out by Webb Research [10]. What follows is a description of steps we have taken to implement Stommel's vision and extend Webb's early ideas into what we believe to be a practical and economical instrument platform.

II. Design Goals and Constraints

Spray is meant to fill the need for a relatively long-lived vehicle to observe ocean physics and biology on the scales of O(100 km) and O(30 day) that characterize the energetic oceanic mesoscale. In trying to define the general circulation, or climate variability like the El Niño-Southern Oscillation (ENSO), mesoscale variability is the main source of competing noise. For biological communities the mesoscale represents an often-dominant perturbation to be observed. The main confusing noises in describing the mesoscale are quasi-diurnal phenomena like the diurnal cycle, internal tides, inertial waves, and weather events. To prevent aliasing mesoscale and higher frequency phenomena into large-scale, low-frequency descriptions, or to resolve the mesoscale, it is necessary to sample on scales of O(10 km) and O(10 h). To describe the typical seasonal state, or to define typical relations occurring on the mesoscale, it is necessary to observe many mesoscale realizations, which translates to years of operation.

The design missions for our glider are a combination of three archetypes: time series, transects, and roving assistants to research cruises. By obviating the need for expensive mooring equipment and research vessels, autonomous gliders should be able to reduce the cost of gathering a time series. Maintaining a

Manuscript received December 27, 1999; revised June 4, 2001. This work was supported by the Office of Naval Research through subcontracts from the Massachusetts Institute of Technology Sea Grant Office.

J. Sherman and R. E. Davis are with the Scripps Institution of Oceanography, La Jolla, CA 92093-0213 USA (e-mail: jtsherman@ucsd.edu).

W. B. Owens and J. Valdes are with the Woods Hole Oceanographic Institution, Woods Hole, MA 02543 USA.

Publisher Item Identifier S 0364-9059(01)09798-9.

station requires a vehicle speed adequate to hold position in the face of ambient currents and a range sufficient to stay on station for extended periods. Where spatial structures or spatially averaged quantities are of interest, gliders can autonomously report a sequence of profiles along a transect, again demanding a speed exceeding ambient currents and a long range. When sophisticated observations are being made from a research vessel, it is often desirable to place these measurements in a broader spatial context, and gliders could carry out adaptive sampling around a ship in rapid response to instructions; here speed is of greater importance and range/duration is less important, but operations over O(30 days) are still needed.

In addition to sampling on scales of O(10 km) and O(10 h) for O(1 year), design goals for Spray are capital and operating costs low enough to permit proliferation of observations in all ice-free ocean environments. To avoid the costs of research vessels, a small glider is needed that is rugged and light enough to be handled without power-assisted equipment from small vessels, like fishing boats. While not envisioned as disposable, the glider's capital cost needs to be low enough, and the data relay complete enough, that an occasional loss can be afforded. This significant design choice makes the glider suitable only for inexpensive sensors. For valuable sensors, a different optimum in the tradeoff between cost and redundancy would result in a different design.

Cost and ease of handling are mainly affected by vehicle size and construction. Operating speed and range are linked to available energy through hydrodynamic drag; higher drag requires higher buoyant forcing to maintain a given speed and thereby uses energy faster. A simple model of unaccelerated gliding elucidates the design features that affect performance. Define the following variables:

ρ	fluid density;
V	vehicle volume;
M	vehicle mass;
B	buoyant force $= g(\rho V - M)$;
A_L	area of wings;
A_D	cross sectional area of hull;
q	vehicle speed;
u	horizontal velocity;
w	vertical velocity;
θ	glide angle (horizontal $= 0$);
x	vehicle range from energy E_0;
L	lift force—normal to vehicle track.
D	drag force—anti-parallel to motion;
C_L	lLift coefficient $L = 1/2\rho A_L C_L q^2$;
C_D	drag coefficient $D = 1/2\rho A_D C_D q^2$.
K	induced drag coefficient.
Λ	performance factor $= KA_DC_D/A_L$;
U_0	reference velocity $= [B/(1/2\rho A_D C_D)]^{1/2}$;
X_0	reference range $= E_0/(1/2\rho A_D C_D u^2)$.

Lift and drag include hydrodynamic forces on wing, hull, and control surfaces. Λ is the key measure of induced drag and gliding performance. U_0 and X_0 are measures of performance in the absence of gliding. U_0 is the speed of a nonlifting vehicle propelled by the thrust B. X_0 is the range the vehicle could obtain with energy E_0 used to power horizontal motion at speed u.

In unaccelerated gliding the total drag balances the along-track component of buoyancy. The total drag is the sum of pressure and skin drags as well as induced drag, a byproduct of generating lift, and can be written (cf. [4]) as

$$D = B\sin\theta = \tfrac{1}{2}\rho q^2(A_D C_D + KA_L C_L^2). \tag{1}$$

For high Reynolds number wings $K \approx \text{Chord}/(\pi\,\text{Span})$; sailplanes have long, slender wings to minimize K while for Spray the induced drag of the hull, in effect a very stubby wing, is significant. In unaccelerated gliding, lift balances the cross-track component of buoyancy, demanding the lift coefficient

$$C_L = B\cos\theta/A_L\frac{1}{2}\rho q^2 \tag{2}$$

and, consequently, setting the total drag coefficient in (1). Substituting (2) into (1) gives a quadratic equation in which profile drag varies as q^2 while induced drag increases as q^{-2}. Solving this relates speed to the glide angle and the performance factor Λ:

$$\begin{aligned} F &= (u/U_0)^2 \\ &= \cos^2\theta\left[\tfrac{1}{2}\sin\theta \pm \sqrt{\frac{1}{4}\sin^2\theta - \Lambda\cos^2\theta}\right]. \end{aligned} \tag{3}$$

The negative square root in (3) corresponds to inefficient, high angle of attack, "behind the power curve," operation where induced drag is dominant. For the desired positive root, decreasing Λ always decreases drag and increases F; this is most important at shallow glide angles, θ, and slow speeds. Range is limited by the stored energy E_0 since the energy $2(B/\rho g)P_{\text{MAX}}$ must be supplied every time the glider reaches its maximum pressure P_{MAX} and must increase its volume to change the buoyancy forcing from $-B$ to $+B$ in order to go up. Since pressure is closely hydrostatic, the average rate of energy supply is Bw. The dimensionless range $x = u\,\delta t$ per unit of energy $Bw\,\delta t$ is then

$$R = (x/X_0) = \frac{\frac{1}{2}\rho A_D C_D u^3}{Bw} = \frac{F}{\tan\theta}. \tag{4}$$

Fig. 1 presents the dimensionless velocity, F, and range, R, versus glide angle. Maximum velocity is achieved at a glide angle steeper than maximizes range. Range is substantially more sensitive to Λ than is speed. The figure does not include the range of small Λ typical of aircraft because the hull drag of neutrally buoyant vehicles makes this impractical to achieve. Consequently, the optimal glide angles are steeper than for aircraft. Equations (3) and (4) and the results in Fig. 1 are well known in aeronautics and the soaring community has used them [7], [8], [9] to devise strategies for extending gliding range and duration driven by vertical motion in the face of winds of differing strengths. For the purpose of ocean glider design we need only some simple observations. First, the drag area $A_D C_D$, as represented in the characteristic speed U_0 and range X_0, is the most important performance determinant. At fixed Λ, both range and the square of vehicle speed increase as $1/A_D C_D$. Hull drag dominates for ocean gliders, so that, having selected vehicle size

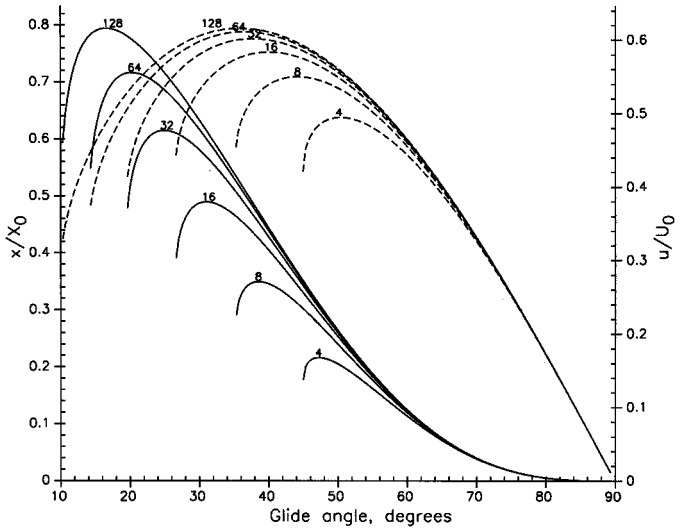

Fig. 1. Theoretical performance of a gliding vehicle as a function of glide angle θ for different performance factors Λ. Dashed lines are horizontal velocity u normalized by the characteristic velocity $U_0 = (2B/\rho A_D C_D)^{1/2}$. Solid lines are range x normalized by $X_0 = E_0/(1/2\rho A_D C_D u^2)$. Numbers are the inverse performance factor $1/\Lambda$. See the text for variables and dynamics considered.

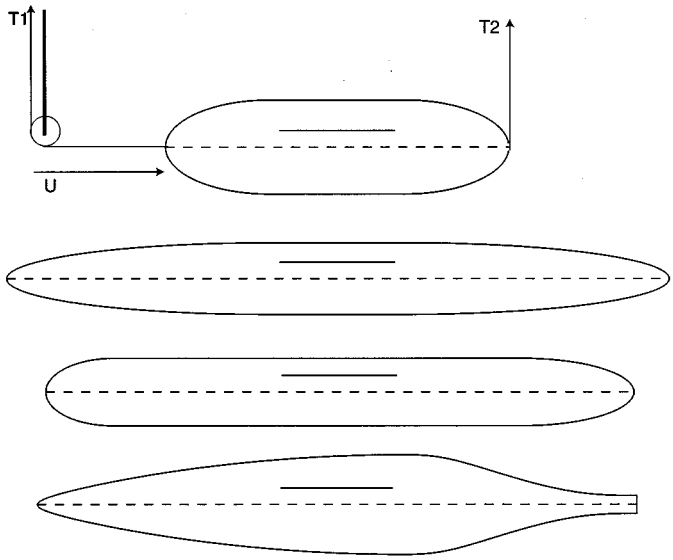

Fig. 2. Cross sections of the four models used for drag tests and schematic of mechanism used to measure drag. The shapes are, from top to bottom, what we call the fat ellipsoid, the slender ellipsoid, the WRC prototype and the UW/APL glider. Horizontal lines inside each figure show the volume-based length $L = V^{1/3}$. The technique of drag measurement is described in the Appendix.

for handling, only the hull shape can be adjusted to improve performance. Second, all other vehicle performance is determined by $\Lambda = KA_D C_D/A_L$. Neglecting induced drag of the hull, $\Lambda \approx A_D C_D/(\pi \text{ Span}^2)$ so that maximum wingspan is favored, within practical limits, so long as the wing area is sufficient to avoid stall (separation of flow over the wing). Because Λ varies as $A_D C_D$ the importance of drag is even greater than indicated by the scaling in U_0 and X_0.

A true performance optimum cannot be achieved for ocean gliders because the range of ocean currents, from a few centimeters per second in the deep ocean to a few meters per second in boundary currents and shallow tidal environments, means that gliding range is critical in some circumstances while speed is key when adverse currents are strong. Operationally the buoyant force B for gliding up or down can be increased to add speed, but it is now impractical to achieve both megameter ranges and m/s speeds with the same small nearly neutrally buoyant vehicle. While induced drag strongly affects range, it has a relatively small effect on maximum speed. Since increasing wingspan to extend still-water range increases $A_D C_D$ and decreases the speed, any choice of wing parameters must be a compromise between optimizing range and speed. Ultimately, Spray's wings were selected to be as long as was structurally desirable and with a chord sufficient to prevent stalling at the highest buoyancy driving and lowest speeds we envisioned. With this choice made, obtaining the lowest drag-area for a given payload and wing geometry became the primary design goal.

In the discussion above, vehicle buoyancy B was treated as a constant. In practice, differences in the compressibility of vehicle and seawater, and ambient density stratification, will lead to ρV, and hence B, varying with depth. Spray is less compressible than seawater so, for example, if its volume is increased by δV at P_{MAX} the buoyancy will be less than $\rho g\, \delta V$ at lower pressures. Increasing vehicle compressibility can reduce this effect, but we have chosen to keep costs down and forego this.

III. Mechanical Design

The paramount importance of drag to performance makes hull shape critical. Initially we were collaborating with Doug Webb of WRC and collectively decided that, in the interests of simplicity and low cost, we would restrict consideration to hulls that were also the vehicle pressure case. Eriksen [1] describes the University of Washington Applied Physics Laboratory (UW/APL) laminar-flow shape that involves a free-flooding hydrodynamic shroud around the pressure case. This design divergence gives the AOSN program the opportunity to assess both approaches. We also set the size of the vehicle to approximately 2 m long with 50-kg mass. This size is about the largest that can be handled at sea without special power-assisted equipment and leads to reasonable operating cost factors such as battery replacement. Assuming that the stored energy E_0 and buoyancy B scale as vehicle volume, scaling up the vehicle size increases the operating speed approximately as $V^{1/6}$ while holding range fixed (neglecting Reynolds Number dependences); at fixed speed, range increases as $V^{1/3}$. This performance gain was not deemed worth the operational penalty of increased size.

As part of this project, in 1995, Webb [2] carried out pool tests of a glider hull designed by WRC. These tests were intended to confirm performance calculations such as those above, but the results were not consistent enough to define the hull drag to better than about 50%. When Spray design began in May 1997, the first step was to measure the drag of the hull shapes depicted in Fig. 2 using the simple procedure outlined in the Appendix. All the shapes were slender cylinders with fore and aft tapering of various degrees of fineness. One had the shape of the WRC prototype tested in 1995; another was the UW/APL laminar flow shape. Eriksen graciously made available to us drawings and drag measurements for the full-scale UW/APL.

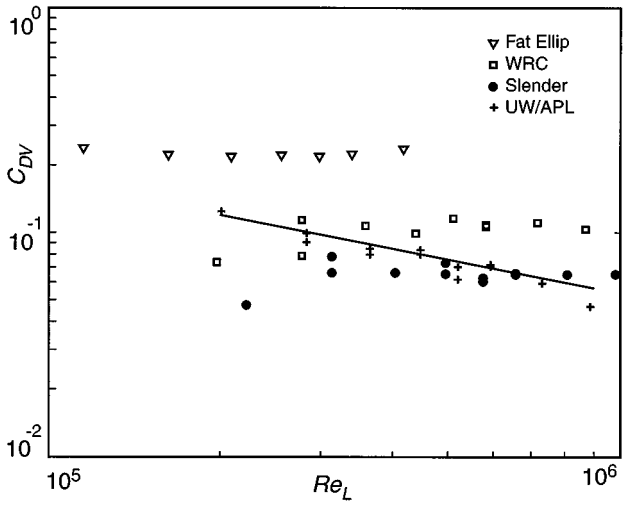

Fig. 3. Measured drag coefficients, based on the useful-volume-based area L^2, for the four half-scale models described in Table I and Fig. 2. The abscissa Reynolds number is the traditional one based on vehicle length. Also shown as a solid line is the drag curve $C_{DV} = 55Re_L^{-1/2}$ measured by UW/APL for their full-scale model. Unlike all the scale models, the full-scale UW/APL model had wings that should make its drag higher than the hull-only models.

Drag results are plotted in Fig. 3 and model dimensions are given in Table I. The C_{DV} drag coefficients in Fig. 3 are based on the area $V_U^{2/3}$ so that models with the same C_{DV} and useful volume have the same drag. For the WRC, UW/APL, and slender ellipsoid (Spray's shape) the useful fraction of volume is taken from the dimensions of the full-scale vehicles; for the fat ellipsoid it was taken equal to the WRC prototype.

All the shapes have approximately constant drag coefficients except the laminar-flow form. The slender ellipsoid has the smallest of the constant drag coefficients, with $C_{DV} \sim 0.075$ (C_{DF} based on frontal cross section is 0.26). The WRC shape is higher by 50% and the fat ellipsoid higher by 500%. The drag coefficient for the UW/APL shape decreases as $Re_L^{-1/2}$ and has approximately the same drag as the slender ellipsoid at $Re_L = 6 \times 10^5$, which for full size vehicles corresponds to a speed near 30 cm/s. Our tests are not accurate enough to define the drag crossover between these models to better than a factor of 1.5. The main conclusions drawn from the drag tests are that: a) improvements can be made on the WRC shape and b) in the range of projected operating speeds the penalty, compared to the laminar-flow shape, for a simpler, more conventional, hydrodynamic shape is small.

After a shape was selected from drag considerations, Spray was designed. At that time (early 1997) we had available for inspection an inoperative prototype of the ALACE Glider designed and built by WRC and adopted some elements from it. The most important was the use of battery packs supported on a central axial column to control gliding. Fig. 4 is a schematic of the design and Table II gives dimensions. The hydraulic system, taken from ALACE, uses a high-pressure pump to move fluid from an internal hydraulic reservoir into an external bladder to increase buoyancy. To reduce buoyancy, a latching hydraulic valve is opened, allowing oil to flow back into the internal reservoir. While the engineering is not unusual, a few elements deserve comment.

Small bubbles in the hydraulic fluid were a stubborn cause of failures in the original ALACE hydraulic system. Despite improved manufacturing and preparation procedures, the system was marginal and even a small bubble ingested into ALACE's reciprocating-piston hydraulic pump caused it to "lose prime" and stop pumping. This results from the pump's relatively low compression ratio. Small bubbles make the hydraulic oil a compressible fluid and, because of a limited compression ratio, the piston cannot increase the fluid's pressure to the ambient exhaust pressure and pumping ceases. Spray's pump is of a different SIO design with a compression ratio greater than 3 : 1 made possible by use of pop-off valves and the absence of ports or hydraulic galleys. Laboratory tests indicate this pump can move relatively dense bubble slurries at high pressure because of both a high compression ratio and the way that entrained bubbles are efficiently directed to the exhaust valve rather than becoming trapped. Selection of elastomeric materials also reduces the rate at which air is absorbed into the Spray hydraulic system.

To reduce manufacturing costs and avoid post-welding heat treatment, the pressure case is built in three segments sealed with O-rings. This permits the nose section, which is critical to low drag, to be machined relatively straightforwardly by a CNC lathe with a 1.25 m bed. The segments are machined from 6061 T6 aluminum bar and tubing. The hull shape is modeled on the slender ellipsoidal cylinder tested for drag with minor modifications to simplify machining. The pressure case has a maximum design depth of 1670 m and has been successfully tested to 1500 m. The general hull thickness of 6.4 mm is thin enough that it would fail from buckling [12] if not stiffened by the hoops that are machined into the hull shape. The hydraulic system is built into the rear pressure-case segment. The main hydraulic components are a flexible internal oil bladder, filter, high-pressure pump, and the latching hydraulic valve controlling flow of oil from the external bladder back into the interior reservoir. This arrangement limits vehicle control because buoyancy can be reduced only while at the surface. Subsequent models will have a three-way valve allowing oil to flow back into the internal reservoir either directly (at low pressure) or through a hydraulic constriction under high pressure. Aside from the hydraulics system, most internal components are mounted to the hull's axial column.

Control of vehicle pitch and roll is accomplished by moving battery packs, which represent the main internal weight. The central pack occupies an approximately 180° segment of the hull cross section and is rotated (full 360°) around the axial column to control roll. The rear pack is moved up to 10 cm longitudinally along the central column to change vehicle pitch (this moves the CG 17 mm). DC motors driving simple rack-and-pinion actuators, with potentiometers to sense position, move these packs. Separating the control of pitch from roll simplifies the actuators and allows efficient battery packaging. Battery packs consist of lithium DD cells but testing was done with alkaline D cells. The center of lift on the wings is approximately 10 cm behind the centers of vehicle mass and buoyancy, far enough to ensure stable response to pitch and speed perturbations but close enough that vehicle pitch is mainly determined by the buoyancy/weight couple and is, therefore, not overly sensitive to vehicle speed.

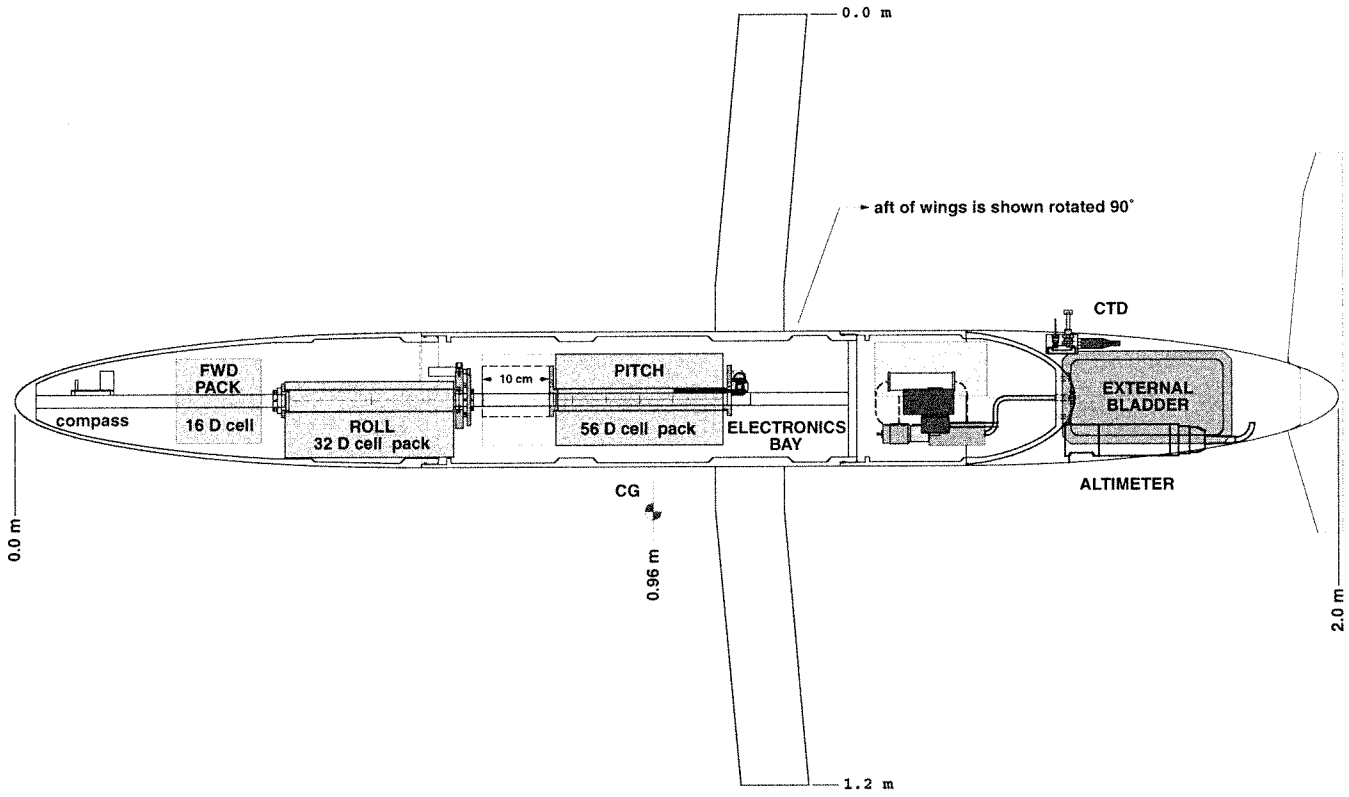

Fig. 4. Schematic of Spray (for dimensions see Table II). The hull is broken into three sections with the hydraulic system in the rear section. Stiffening hoops machined into the hull prevent buckling failure under pressure. Movable batteries are suspended from the axial column, as are the compass and controller electronics. Bulkhead connectors provide access to sensors in the flooded rear section. GPS and ORBCOMM antennas are built into a wing that is rolled vertical when the vehicle is on the surface.

TABLE I
DIMENSIONS OF FOUR HALF-SCALE MODELS WHOSE DRAG WAS MEASURED. USEFUL VOLUME, V_U, IS THE VOLUME OF THE PRESSURE-CASE HULL. THE CHARACTERISTIC AREA $L^2 = V_U^{2/3}$ IS USED TO DEFINE DRAG COEFFICIENTS C_{DV}

Hull Shape	Length cm	Diameter cm	Exterior Volume cc	Useful Volume cc	Area Wetted sq cm	Vol-Based L cm
UW/APL	91.4	15.2	8410	5200	2838	17.32
WRC	89.7	10.4	6800	5860	2731	18.03
Fat Ellipse	52.3	14.4	6800	5860	2061	18.03
Slender	101.1	11.0	7090	5850	2906	18.02

The aft end of the pressure case is rounded to retain a high strength-to-weight ratio and is penetrated by a hydraulic line to the external bladders and by bulkhead underwater electrical connectors. A solid polypropylene fairing covers the aft pressure case, extending Spray's ellipsoidal shape, and is hollowed out to house the external displacement-changing bladders and to provide room for various operational and scientific sensors (see below). It also supports the vertical stabilizer to which an antenna for a secondary radio beacon has been mounted. In shaping the interior of the solid aft section, care was taken to preclude air from being trapped inside and possibly preventing the surfaced vehicle from submerging. For early field trials, the flooded aft section housed a safety drop weight, acoustic altimeter, radio beacon for emergency recovery, and an acoustic pinger for underwater tracking, as described below.

IV. ELECTRICAL DESIGN AND SENSORS

The controller and associated electronic subsystems deal with attitude and buoyancy control, interrogation and command of scientific sensors, processing and storing data, navigation and satellite communication, and a fail-safe watchdog system. Except for the latter, these functions are under control of one processor (Onset TT8) with auxiliary boards supporting the necessary drivers and analog sections.

In-flight glide control is based on measured pitch, roll, heading, pressure, and altitude above the bottom used in the

TABLE II
MEASURES AND DIMENSIONS OF SPRAY. WING AND VERTICAL STABILIZER LENGTHS ARE OF THE LIFTING SURFACES, EXCLUDING INTERVENING WIDTHS OF HULL AND TAIL CONE. THE EXTERNAL VOLUME INCLUDES THE FLOODED VOLUME IN THE TAIL CONE. THICKNESS OF WING AND STABILIZER ARE 4 AND 3.2 mm, RESPECTIVELY

Hull Length	200 cm
Hull Diameter	20.3 cm
Volume, external and pressure hull	52000 cc, 43000 cc
Wing, Half-Length and average chord	49 cm, 10.2
Vertical Stabilizer, Length and chord	46 cm, 7 cm
Total Mass	50.2 kg
Pressure Case	6061 T6 Aluminum, 19.7 kg
Hydraulic System Max Volume Change Energy Efficiency	3.4 kg 900 cc 50% @ 1000 dbar
Batteries Energy	52 DD Li CSC cells, 12 kg 13 MJ
Science Payload	3.3 kg
Life Time:	1000 cycles to 1500 m pumping 300 cc
GPS Navigation	±100 m
ORBCOMM Satellite Link	Two-way. 25 bytes per minute average.

flight control algorithms. A Precision Navigation compass (TCM2, located in the nose as shown in Fig. 4) supplies pitch, roll and heading. Pressure is measured for glide-control and scientific purposes with a Paines 211-38 pressure gauge. A Tritech PA-200 acoustic altimeter gives distance to the bottom (up to its 80-m range). Pitch and roll are adjusted every 40 s based on the measured pitch and heading errors. The pitch control algorithm is a straight proportional loop, with low gain to produce an over-damped response toward the desired pitch angle. The set-point for heading control includes a term proportional to a fading-memory integral of heading error. This serves to minimize the error of the average heading from the desired value. During the Monterey underwater canyon operation described below, the standard deviations from the desired pitch and heading averaged 0.5° and 3°, respectively.

To end a downward glide, buoyancy is increased either upon reaching a pre-programmed depth, after a set time, or in proximity to the bottom. When the hydraulic pump is started, ballast is moved to produce shallower pitch and glide angles in order to minimize overshooting the set depth. When the Spray begins to ascend, a pitch angle is assumed to optimize the upward glide. Typical turn-around requires 4 m in depth between where the pump is started and ascent begins. Pump current and voltage are monitored for undervoltage or overcurrent faults, which cause a mission abort.

Scientific sensors presently include the pressure gauge used for glide control, a Sea-Bird Electronics 70 ms response thermistor probe, and a Precision Measurement Engineering conductivity sensor. The conductivity sensor, a $1 \times 5 \times 25$ mm ceramic substrate with a four-electrode cell at its tip has good flushing, low drag, and a small sampling volume (fast response). The cell is, however, easily affected by particles in the water and during the Monterey trial, several times it became temporarily fouled, apparently as the result of encounters with biological aggregates for which Monterey Bay is well known. The C and T sensors are physically located on top of the flooded tail section, 40 cm forward of the stern. The pressure port is at the aft end of the pressure case, with the sensor itself thermally isolated by 10 cm section of 3 mm tubing.

The P, C, and T signals are sampled every 5 s by a 16 bit a/d and the data stored. One channel is available for expansion. For each dive-cycle, all data are stored in RAM, processed for satellite telemetry, and then RAM is reset for the next dive. As a back-up measure, and to allow storage of more data than are telemetered, a Persistor Instruments CF1 with 96 Mbyte flash memory stores a serial stream from the TT8. For the Monterey operation this allowed post-analysis of the complete 5 s interval data set.

Position on the surface is measured with an Ashtech G8 GPS unit with a 25-dB-gain preamplifier. In the Monterey trial, fixes were acquired, on average, 70 s after powering on the unit. Location is obtained at the time of initial surfacing, and again at the start of the next dive cycle. A simple navigation algorithm computes distance and heading from the GPS fix to the desired waypoint assuming a constant pitch, heading, and attack angle, and neglecting currents. This heading is taken unless the waypoint is close, in which case Spray glides up and down with a constant roll in a $\sim$50-m circle.

Communications with ORBCOMM and reception of GPS signals uses a dual element antenna embedded in one of the wings that is rolled vertical when the Spray surfaces. One antenna element is a quarter-wave ORBCOMM antenna using the hull as a counterpoise. The second element is a half-wave GPS antenna in the tip of the wing to provide best water clearance. The antennas and an aluminum header are potted in urethane using a mold that also defines the wing shape. The wings used in Monterey were of uniform 4 mm thickness. Subsequently a thicker airfoil shape has been adopted to simplify construction, provide greater wing stiffness to protect electrical integrity of the enclosed antennas, and perhaps to even decrease hydrodynamic drag.

Data and new mission instructions are telemetered using the ORBCOMM communications system. The spaceborne portion of the ORBCOMM system is a constellation of low-earth-orbit satellites, 24 satellites at the time of the Monterey field trials eventually expanding to 44. Data flows to these satellites, then to Gateway Earth Stations (GES) that forward it to Gateway Control Centers that provide access to the users via email. Commands for Spray follow this path reversed.

Spray uses a Panasonics KX-G7100 Subscriber Communicator (SC, a transceiver) to communicate with ORBCOMM satellites. The SC transmits or receives data after it has been polled by a satellite. In Monterey this happened about every minute. The SC transmits data to the satellite at 2400 baud using the 148–150-MHz band and receives data at 4800 baud in the 137–138-MHz band. When the SC and a GES are both within the footprint of a satellite, then messages up to a practical limit of 3 to 8 Kbytes can be sent from the SC back to the GES in "bent-pipe" mode. A GES in Arizona provided "bent pipe" coverage during more than 90% of the Monterey operation.

When only the SC is in the footprint of the satellite, messages (Globalgrams) are limited in length to 229 bytes that are stored in the satellite and forwarded when the satellite sees GES. For the Monterey test, only a few messages were Globalgrams.

Each time Spray surfaced 30 min were allocated for transmitting 1 kB in 9 messages. These messages included glider position, engineering data, and pressure, temperature, and conductivity for profiles. For three of the 98 profiles, the satellite coverage was at low angles and precluded complete data transmission in 30 min. Commands were sent to Spray using short emails that ORBCOMM relayed to Spray. During the Monterey trial the sampling rate was changed. Other commands could change the waypoint for Spray or modify other parameters of the mission. At the end of the sustained deployment, a command to abort the mission was relayed to Spray to schedule recovery during daylight and good weather.

Because Spray is an unproven instrument, a robust emergency back-up system is implemented. A drop weight allows the glider to surface in case of hydraulics failure. An RF beacon with a separate antenna on the vertical stabilizer allows surface locating in the event ORBCOMM communication is not successful. An acoustic pinger (Datasonics ALP-365) allows subsurface tracking from onboard ship. Lastly, a separate processor (Parallax Stamp module) is used as a watchdog for the TT8. If the TT8 supplies no heartbeat (set at a 10-min duty cycle), the watchdog activates the drop weight, turns on the RF beacon, and resets the TT8, which goes into an abort/recovery mode.

V. Field Trails

In mid-August 1999 the Autonomous Ocean Sensing Network (AOSN) program mounted an experiment in the Monterey underwater canyon that was meant to involve all the program's autonomous vehicles, including its newly developed autonomous gliders. The scientific goal of this experiment was to explore how the internal tide evolves as it propagates from relatively deep water into the canyon to form strong tidal bores as the canyon becomes shallow. High operating speeds (several knots) were needed to explore the strong-current part of this phenomenon, so the autonomous gliders were scheduled to maintain time series stations in deeper parts of the canyon where tidal velocities were not large. Since this was the first extended mission for Spray, the simple operational plan of maintaining station was a good opportunity to explore both the capabilities of this new kind of instrument and to prove the performance of our particular implementation.

Spray's nominal measuring location was a site in the Monterey underwater canyon (see Fig. 5) with a relatively flat bottom at 380 m depth and steep canyon walls located about 1.5 km away. On August 26, 1999, the prototype Spray was deployed 10 km west of its planned site, found her way to that location, and began profiling and station keeping. Eleven days later Spray was recovered without intervening attendance after collecting a time series of 182 temperature and conductivity profiles.

How well did we achieve the goal of low drag? Spray's drag performance was estimated from its known buoyancy and from measurements of its pitch angle φ and vertical velocity, w, inferred from pressure measurements. The along-track force balance is

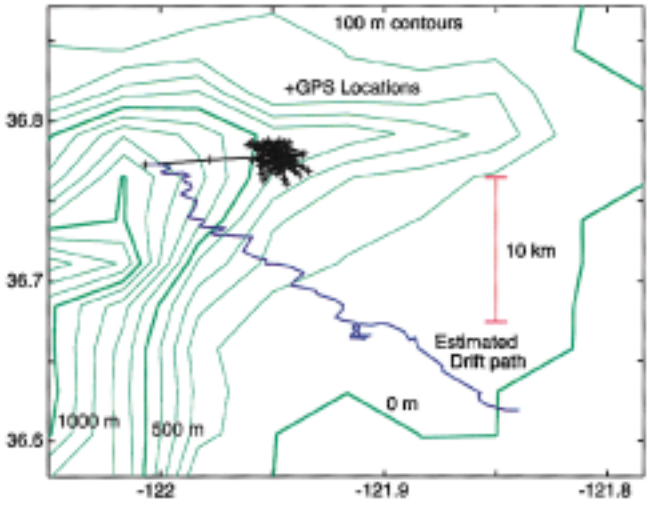

Fig. 5. The setting of operations in the Monterey underwater canyon. Black lines show track of Spray starting 10 km west of the programmed station location; a cross marks each surfacing position. Blue line is a progressive vector diagram of the vertically averaged current inferred from the difference between dead reckoning and actual positions over each profiling cycle. This shows tidal motion and a westward 3 cm/s drift. Green lines show low-resolution bathymetry with 100 m contour interval and thick lines at 500 and 1000 m.

$$\begin{aligned} B\sin\theta &= \frac{1}{2}\rho A_{\mathrm{CROSS}} C_{\mathrm{TOT}} \frac{w^2}{\sin^2\theta} \\ &= \frac{1}{2}\rho\left(A_{\mathrm{CROSS}} C_{\mathrm{DF}} + A_{\mathrm{SKIN}} C_{\mathrm{SKIN}} + K A_{\mathrm{LIFT}} C_{\mathrm{LIFT}}^2\right) \\ &\quad \cdot \frac{w^2}{\sin^2\theta} \end{aligned} \tag{5}$$

where the first term on the right side represents pressure and skin drag on the hull (C_{DF} is based on the hull cross section), the second term represents skin drag on the wings and vertical stabilizer, and the third term represents the induced drag on both the wings and the hull. The term $w/\sin\theta$ is the speed q. The middle expression simply defines C_{TOT} as the total drag coefficient based on the cross-sectional area.

The cross-track force balance relates buoyancy to the upwards component of lift and determines the angle of attack α (between the relative flow and the hull axis) to produce the needed lift. From the lift line of the wings and hull from Hoerner and Borst [3], we estimate α for the Monterey Canyon trials as 3.4°, which is consistent with attempts in earlier field tests to measure the angle of attack directly with a mechanical vane. Measured pitch and estimated angle of attack determine the glide angle θ and allows speed q to be computed from vertical velocity w measured through pressure. With this, buoyancy (known to about 10 g) defines the total drag and C_{TOT}. Empirical results in Hoerner [4] allow the skin friction and induced drag to be estimated and the hull drag estimated by subtraction. Velocity and pitch were averaged over the first ten

TABLE III
DRAG PERFORMANCE IN THE MONTEREY CANYON FIELD TRIAL. FIRST 3 COLUMNS ARE BUOYANCY IN GRAMS, PITCH φ, AND VERTICAL VELOCITY w, ALL OF WHICH WERE MEASURED. COLUMNS 4–6 ARE GLIDE ANGLE θ, TOTAL DRAG COEFFICIENT AND HORIZONTAL VELOCITY u, ALL OF WHICH DEPEND ON ESTIMATES OF THE ANGLE OF ATTACK. COLUMN 5 IS THE INFERRED HULL DRAG COEFFICIENT, C_{DF}, BASED ON FRONTAL AREA. THE LAST COLUMNS ARE THE FRACTIONS OF DRAG ASCRIBED TO SKIN FRICTION ON THE WINGS AND VERTICAL STABILIZER, AND TO INDUCED DRAG ON THE HULL AND WINGS. THESE LAST 3 COLUMNS DEPEND ON MODEL ESTIMATES OF VARIOUS DRAG COEFFICIENTS OF THE VEHICLE. THESE RESULTS ARE FROM THE FIRST 10 DIVE CYCLES BUT 10-CYCLE AVERAGES DIFFER BY ONLY 5%

B/g gm	φ deg	w cm/s	θ deg	C_{TOT}	u cm/s	C_{DF}	Skin	Induced
-103	16.5	-7.7	19.9	0.40	21.3	0.29	21%	9%
160	16.7	9.7	20.1	0.40	26.5	0.28	21%	9%

TABLE IV
PREDICTED PERFORMANCE FOR SPRAY BASED ON DRAG MEASURED IN MONTEREY UNDERWATER CANYON AND A 13 MJ ENERGY SUPPLY. THE GLIDE ANGLE 36.0° MAXIMIZES HORIZONTAL VELOCITY u FOR FIXED B WHILE 18.3° MAXIMIZES RANGE. THE LISTED RANGE ASSUMES 25% OF ENERGY IS NOT USED FOR PROPULSION

Buoyancy, B/g	100 gm			300 gm		
Glide Angle, θ (deg)	18.3	25.0	36.0	18.3	25.0	36.0
Horizontal, u (cm/s)	20.0	22.8	24.4	34.6	39.5	42.3
Life in cycles	1016	1102	1171	660	677	695
Range, x (km)	6144	4726	3223	3993	2897	1911

dive cycles from the 150- and 325-m depth range, over which Spray appeared to be in steady motion. Buoyancy was estimated from profiles of temperature and salinity, measurements of Spray's compressibility, ballasting measurements with the bladder empty, and (for the buoyancy during ascent) the measured pumping energy and known pump efficiency. Table III shows the results.

While the inferred w, which should be a relative velocity, is subject to errors from internal waves, the main uncertainty in the total drag coefficient is uncertainty in the wing lift coefficient which determines the inferred angle of attack α and hence the glide angle θ; we estimate the uncertainty in C_{TOT} to be 15%. The apportionment of drag into hull drag, skin drag on wings and stabilizer, and induced drag depends on the empirical results from which these forces were modeled and we do not know their errors. We note, however, that the drag coefficient based on frontal area, C_{DF}, from the Monterey trial is only 15% higher than the tow-tank, half-scale measurement.

The results from Monterey can be used to determine the lumped drag and lift coefficients in the drag law (1). Based on Spray's frontal cross section of $A_D = 324$ cm^2 and wing area $A_L = 980$ cm^2, the results in Table III translate to $C_D = 0.37$, $K = 0.09$, and Λ near 1/90. To convert these dynamical parameters into a predicted operating range it is necessary to know the stored energy, the mechanical conversion efficiency (both in Table II), and the drains on stored energy other than buoyancy generation. At the surface the pump is run to provide extra buoyancy to keep the antenna exposed; this takes about 2.9 kJ per cycle. Transmission of T and S profiles from up and down profiles consumes about 1 kJ per cycle while GPS locating uses less than 100 J per fix. The present sensors and data collecting have not been optimized for power consumption. Control, sensors, and data management now consume about 150 mW but we believe this can easily be reduced to 90 mW. Additionally, in order to compensate for the difference in compressibility of Spray and seawater, it is necessary to pump approximately 100 cc more than the theoretical volume $2B/g\rho$. Even with this penalty, in operating to 1000-m depth, slightly less than half the stored energy is used for high-pressure pumping.

Because some of the uses of stored energy are on a per-cycle basis while others scale as time, and because hydrodynamic efficiency is a complex function of θ, calculation of range cannot be reduced to a simple formula. Based on the hydrodynamic performance deduced in Monterey, and taking into account the other energy uses, including surfacing and transmitting every other cycle and providing 90 mW for control and sensors, Table IV presents projected performance for some reasonable operating conditions.

VI. INTERNAL VARIABILITY IN MONTEREY CANYON

The effect of canyon bathymetry on the internal tide was investigated by analyzing the vertical displacement of isotherms, η. Displacements were calculated with respect to a mean temperature profile calculated over the 11-day time series (Fig. 6). If an isotherm went deeper than the profile, its depth was held constant at its last valid value, resulting in the horizontal lines in Fig. 7. This biases variance estimates low for the deepest isotherms where data gaps are most frequent. The depth region between 50–350 m is explored, where the Vaisala frequency, N, is nearly constant.

Frequency spectra (Fig. 8) were computed for three depth bands: 50–150 m (shallow), 150–250 m (intermediate), and 250–350 m (deep). These spectra suffer from high-frequency aliasing because of the 3-hour interval between profiles. However, a strong bottom intensified tidal signature is quite apparent. The shallow range has no discernible peaks in the tidal frequency band. The intermediate depth range shows a strong peak at the diurnal frequency (0.042 cph) but little energy at the semi-diurnal tide (0.081 cph). The deep region is the only one that has a strong M2 spectral peak. Plotting the rms η for frequencies >0.03 cph as a function of depth (Fig. 6) shows strong bottom intensification. According to the customary WKB scaling, η should scale as $N^{-1/2}$. The Garret–Munk model (cf. [5]) gives an rms η of 7 m for $N = 3$ cph for the open ocean. The observed deep values approach three times the expected GM level.

Although the above analysis clearly shows that the tidal signal is bottom trapped, Fig. 7 also suggests that there is strong variability in the amplitude of the tidal signals over the 11-day deployment. For the first 7 days of the record, the vertical temperature structure appears to be constant. During the last 3–4 days, the vertical structure changes. The stratification becomes more bottom intensified and the isotherms that were near 100 m depth are displaced downward by O(100 m). The cause of this change is not apparent, but may be due to the propagation of an eddy

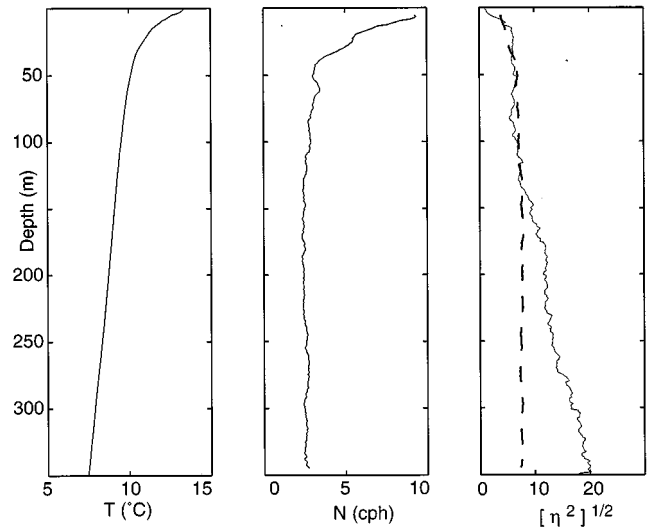

Fig. 6. Eleven-day mean temperature profile at Spray's Monterey Canyon site (left). The mean Vaisala frequency (center) is computed from profiles of temperature and salinity. On the right, the solid line is rms vertical displacement after high-pass filtering above 0.03 cph and the dashed line is the displacement predicted by the Garret–Munk. The amplitude is bottom-intensified nearly three times over that predicted.

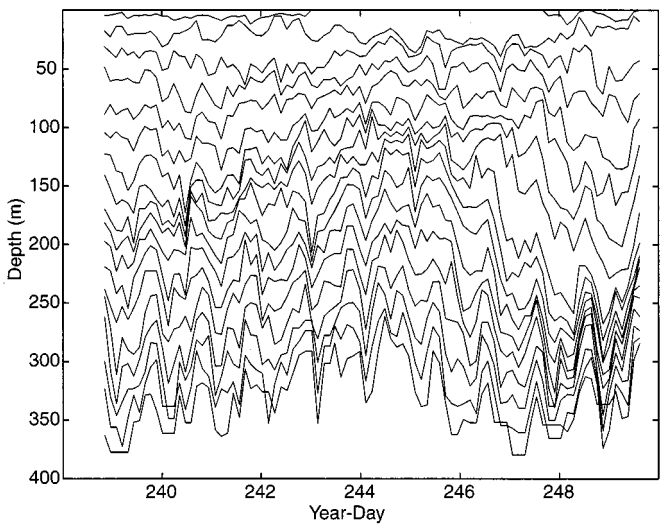

Fig. 7. Isotherms depths computed from descending profiles only. Only isotherms separated by approximately 20 m are shown. Note the lack of the tidal signature above 50 m compared to the tide's strong presence at depth.

into the region or a meander in the offshore California Current. At the same time, the amplitude of the deep tidal signal appears to increase.

Previously, Petruncio *et al.* [6] observed strong tidal bores further inshore along the axis of the canyon. Although the bores appeared at the same phase in the tidal cycle, they did not appear to be correlated with the astronomical variations in the tide. The Spray time series suggests that offshore influences on the vertical stratification may play a significant role in determining the strength of the bottom intensified M2 tidal signal and, therefore, the appearance of the tidal bore.

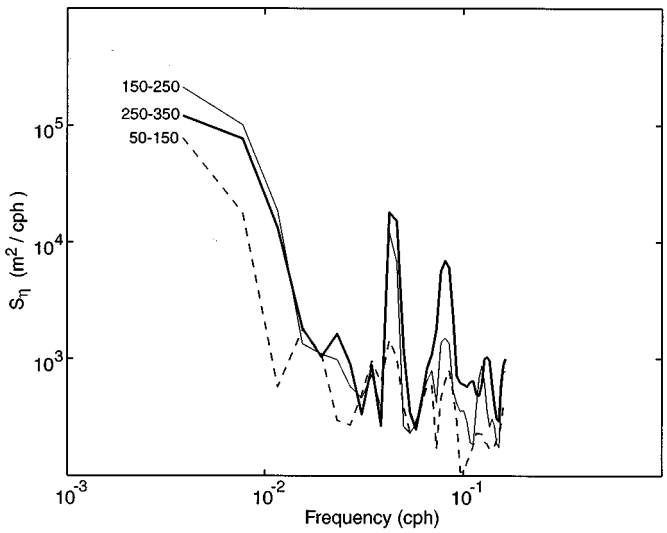

Fig. 8. Frequency spectra of η computed over 100 m depth bands. Three-hour sample interval results in Nyquist-aliasing of high-frequency internal waves. The 50–150 m average spectrum shows little tidal energy. The intermediate depth (150–250 m) shows a strong diurnal component and little semi-diurnal energy, while the near-bottom region (250–350 m) has large semi-diurnal peak and diurnal peaks.

VII. Conclusion

The Spray is a successful implementation of Henry Stommel's vision of small, long-lived underwater gliders. Based on the drag measured in the Monterey trial and conventional estimates of the induced drag it is possible to predict Spray's performance on long-term missions. Table IV gives some combinations of buoyancy forcing, glide angle, horizontal velocity and range that Spray can achieve. Spray's low maximum speed will limit the missions, but the overall capabilities will allow a wide range of long-term sampling missions, including time-series stations and autonomous transects. While it is difficult to project from a prototype, construction cost should be near $25 000. The ability to deploy and recover simply should make the cost of a mission a fraction of the construction cost.

The Monterey tests of Spray demonstrate that vehicle performance will make possible extended long-term and long-range missions. These tests also demonstrate satellite relay of kilobytes of data per hour, robust two-way communications, and rapid positioning on demand. While data throughput may degrade when data relay is not in bent-pipe mode, the same configuration and software used in Monterey can be used anywhere, making feasible global operation of Spray and related autonomous vehicles, such as profiling floats.

Analyses of the data obtained from Spray are consistent with previous time series taken in the vicinity of the Monterey Canyon. Spray's profile data have shown a strong baroclinic diurnal signal at a latitude where the Coriolis frequency is higher than diurnal ($f = 0.05$ cph), suggesting that there is a local source. This is consistent with measurements further offshore where increased mixing suggests that the barotropic tide is interacting with steep topography to generate increased internal wave energy.

APPENDIX
LABORATORY DRAG MEASUREMENTS

In the process of selecting a hull shape for Spray, the drags of roughly half-scale (1 m long) cylinders of the shapes shown in Fig. 2 were measured. The procedure used an accurately controlled tow cart that operated over quiescent water in a 1.5-m square cross section tow tank. The cart towed models through the tank at speeds between 10 and 100 cm/s. The models were ballasted to be slightly negatively buoyant and were suspended from a vertical pylon extending down from the tow cart by a thin, nominally horizontal, line to the model nose, and from a nominally vertical line to the model tail (see schematic in Fig. 2). Tensions were measured in both lines with load cells, as was the angle of the aft line. These data were used to calculate the drag force by averaging results over periods of steady motion.

Two imperfections in this procedure limited its accuracy. Some models at high speed had a tendency to swerve ("fish tail") around a straight course. The associated lateral forces and the induced drag contaminate measurements of hull drag. Tuning the model buoyancy and the length and angle of the aft line reduced this contamination. Also, the pulley and lower end of the forward pylon disturbed the water through which the model then moved. This contaminated drag measurements, and perhaps most seriously affected the laminar-flow UW/APL design, but hopefully affected all models similarly and therefore did not upset the relative drags of different shapes.

ACKNOWLEDGMENT

The authors would like to thank to Dr. T. Curtin whose vision led to the AOSN program and who provided the flexibility to make it a success, and to Dr. J. Bellingham who made it run.

REFERENCES

[1] C. C. Eriksen, T. J. Osse, R. D. Light, T. Wen, T. W. Lehman, P. L. Sabin, J. W. Ballard, and A. M. Chiodi, "Seaglider: A long-range autonomous underwater vehicle for oceanographic research," *IEEE J. Oceanic Eng.*, vol. 26, pp. 424–436, Oct. 2001.

[2] D. Webb, *ALACE Glider—Test Tank Trials*. Falmouth, MA: Report of the Webb Research Corp., 1995.

[3] S. F. Hoerner and H. V. Borst, *Fluid-Dynamic Lift: Practical Information on Aerodynamic and Hydrodynamic Lift*. Brick Town, NJ: Hoerner, 1975.

[4] S. F. Hoerner, *Fluid-Dynamic Drag; Practical Information on Aerodynamic Drag and Hydrodynamic Resistance*. Brick Town, NJ: Hoerner, 1965.

[5] W. Munk, *Evolution of Physical Oceanography*, B. A. Warren and C. Wunsch, Eds. Cambridge, MA: MIT Press, 1981, pp. 264–291, 623.

[6] E. T. Petruncio, L. K. Rosenfeld, and J. D. Paduan, "Observations of the internal tide in Monterey Canyon," *J. Phys. Oceanogr.*, vol. 28, pp. 1873–1903, 1998.

[7] P. B. MacCready, "Understanding speed-to-fly and the speed ring," *Soaring*, vol. 47, no. 5, pp. 42–47, 1982.

[8] S. A. Jenkins and J. Wasyl, "Optimization of glides for constant wind fields and course headings," *J. Aircraft*, vol. 27, no. 7, pp. 632–638, 1990.

[9] P. B. MacCready, "Optimum airspeed selector," *Soaring*, vol. 18, no. 2, pp. 16–21, 1954.

[10] P. Simonetti, "SLOCUM Glider Design," Webb Research Corp., Falmouth, MA, Rep. Webb Research Corp., 1992.

[11] H. Stommel, "The Slocum Mission," *Oceanography*, vol. 2, no. 1, pp. 22–25, 1989.

[12] J. F. Harvey, *Theory and Design of Pressure Vessels*. New York: Van Nortrand Reinhold Company, 1985, p. 623.

[13] R. E. Davis, D. C. Webb, L. A. Regier, and J. Dufour, "The autonomous Lagrangian circulation explorer (ALACE)," *J. Atm. Oceanic Tech.*, vol. 9, no. 3, pp. 264–285, 1992.

Jeff Sherman received the B.A. degree in applied mechanics from the University of California at San Diego (UCSD), La Jolla, in 1981 and the Ph.D. degree in applied ocean sciences from Scripps Institution of Oceanography, UCSD, in 1989.

He has continued on at Scripps, presently as a specialist in the Physical Oceanography Research Department. His research interests include instrumentation, ocean mixing, and *in-situ* observations of shoaling surface waves.

Russ E. Davis, photograph and biography not available at the time of publication.

W. B. Owens, photograph and biography not available at the time of publication.

J. Valdes, photograph and biography not available at the time of publication.